Liquid-Feed Flame Spray Pyrolysis of Metalloorganic and Inorganic Alumina Sources in the Production of Nanoalumina Powders

T. Hinklin,[†] B. Toury,[‡] C. Gervais,[‡] F. Babonneau,[‡] J. J. Gislason,[§] R. W. Morton,[§] and R. M. Laine*,[†]

Department of Materials Science and Engineering, University of Michigan, Ann Arbor, Michigan 48109-2136, Laboratoire de la Matière Condensée, Université Pierre et Marie Curie/CNRS, 4 place Jussieu, Paris, France, and ConocoPhillips Petroleum Co., 92E Bartlesville Technical Center, Bartlesville, Oklahoma 74004

Received December 10, 2002. Revised Manuscript Received August 1, 2003

Liquid-feed flame spray pyrolysis (LFFSP) of metalloorganic [$N(CH_2CH_2O)_3Al$, alumatrane, and $Al(Acac)_3$] and inorganic alumina [$AlCl_3$ and $Al(NO_3)_3{\cdot}9H_2O$] precursors dissolved in 1:1 ethanol/THF, aerosolized with O_2 and ignited can produce quite different alumina nanopowders during the ensuing combustion process. The metalloorganics appear to volatilize and combust easily to give nano-alumina, with particle sizes <20 nm and corresponding surface areas of ≈60 m^2/g at rates of 50 g/h. In contrast, the nitrate appears to melt during combustion rather than volatilize, forming large, hollow particles typical of a spray pyrolysis process with particle sizes >70 nm and surface areas of ≈12 m^2/g. $AlCl_3$ appears to volatilize easily but does not hydrolyze rapidly in the flame leading to mixtures of alumina and recovered $AlCl_3$. The resulting nanopowders consist of a mixture of transition alumina phases, primarily δ^*, that could only be successfully identified and quantified by Rietveld refinement. Because the δ phase is not typically made as a high-surface-area material or in large quantities, it offers the opportunity to serve as a novel catalyst support. On heating to 1000 °C, the dominant phase becomes θ-Al_2O_3 that was clearly identified by ^{27}Al MAS NMR using ab initio calculations of the ^{27}Al NMR parameters derived from the X-ray structure. At present, the exact mechanism(s) whereby particles nucleate and grow, and phases form from the species generated during combustion, remains unknown.

Introduction

The advent of the "nano-age" has prompted intense research into the design and synthesis of nanotools and devices for diverse applications. Mostly unknown to the world at large, the ceramics community has long been a participant in "nanotechnology," through the production of kiloton quantities of fumed silica, titania, and alumina from flame spray hydrolysis of the respective metal chloride gases.[1−4]

One oft-noted problem with flame hydrolysis processing has been the inability to produce mixed-metal oxide powders with complete control of composition and phase.[1,3] In part, the lack of success in producing mixed-metal oxides via flame hydrolysis comes from the disparate rates of hydrolysis of various metal chlorides which leads to different rates of particle nucleation and growth in the flame. In part, the lack of volatile metal chlorides of many metals reduces the number of mixed-metal systems that are potentially accessible.

We recently developed an alternate synthetic approach to single and mixed-metal oxide nanopowders using low-cost, mixed-metal alkoxide precursors made directly from metal oxides and hydroxides.[5,6] As reported earlier, these alcohol-soluble precursors can be aerosolized with O_2, and the resulting vapor can be ignited to produce combustion with flame temperatures >1500 °C.[7−13] We term this process liquid-feed flame spray

* To whom correspondence should be addressed. Phone: 734-764-6203. Fax: 734-763-4788. E-mail: talsdad@umich.edu.
† University of Michigan.
‡ Université Pierre et Marie Curie/CNRS.
§ ConocoPhillips Petroleum Co.

(1) Ulrich, G. D. *Chem. Eng. News* **1984**, *62*, 22.
(2) Ichinose, N.; Ozaki, Y.; Kashu, S. *Superfine Particle Technology*; Springer-Verlag: London, 1992.
(3) Gurav, A.; Kodas, T.; Pluym, T.; Xiong, Y. *Aerosol Sci. Technol.* **1993**, *19*, 411.
(4) Pratsinis, S. E. *Prog. In Energy Combust. Sci.* **1998**, *24*, 197.
(5) a. Laine, R. M.; Treadwell, D. R.; Mueller, B. L.; Bickmore, C. R.; Waldner, K. F.; Hinklin, T. *J. Chem. Mater.* **1996**, *6*, 1441. b. Waldner, K.; Laine, R. M.; Bickmore, C.; Dumrhongvaraporn, S.; Tayaniphan, S. *Chem. Mater.* **1996**, *8*, 2850.
(6) a. Laine, R. M.; Mueller, B. L.; Hinklin, T. U.S. Patent 5,418,-298, May 23, 1995. b. Laine, R. M.; Waldner, K.; Bickmore, C.; Treadwell, D. U.S. Patent 5,614,596, March, 1997.
(7) Bickmore, C. R.; Waldner, K. F.; Treadwell, D. R.; Laine, R. M. *J. Am. Ceram. Soc.* **1996**, *79*, 1419.
(8) Baranwal, R.; Villar, M. P.; Garcia, R.; Laine, R. M. *J. Am. Ceram. Soc.* **2001**, *84*, 951.
(9) Sutorik, A. C.; Neo, S. S.; Hinklin, T.; Baranwal, R.; Treadwell, D. R.; Narayanan, R.; Laine, R. M. *J. Am. Ceram. Soc.* **1998**, *81*, 1477.
(10) Bickmore, C. R.; Waldner, K. F.; Baranwal, R.; Hinklin, T.; Treadwell, D. R.; Laine, R. M. *J. Eur. Ceram. Soc.* **1998**, *18*, 287.
(11) Sutorik, A. C.; Baliat, M. S. *J. Metastable Nanocryst. Mater.* **2002**, *13*, 371.
(12) Laine, R. M.; Waldner, K.; Bickmore, C.; Treadwell, D. R. U.S. Patent 5,958,361, Sept. 28, 1999.
(13) Laine, R. M.; Hinklin, T.; Williams, G.; Rand, S. C. In *Materials Science Forum* Vols. 343−346; Scitec & Trans Tech Publications: Zurich, Switzerland, 2000; pp 500−10.

10.1021/cm021782t CCC: $27.50
Published on Web 12/16/2003

pyrolysis (LFFSP). Related forms of LFFSP production of mixed-metal oxide materials and nanopowders have been reported.[4,14,15]

In LFFSP, if combustion is quenched rapidly, the resulting "soot" consists of nanopowders with the exact composition of the precursor solution.[8,10] The particle sizes and size distributions are partially a function of solution concentration but are best controlled by the quench rate. Typical average particle sizes (APSs) are currently less than 50 nm.

We have previously reported the LFFSP production of spinel ($MgAl_2O_4$),[7] mullite ($2SiO_2 \cdot 3Al_2O_3$),[8] and β''-alumina ($Na_2O \cdot 11Al_2O_3$)[9] and benchmarked our process against gas feed, flame spray hydrolytically produced titania.[10] Recently, Sutorik and Baliat were able to use LFFSP to produce $Ce_xZr_{1-x}O_2$ solid solutions.[11]

On the basis of our LFFSP titania studies, which gave materials identical (85% anatase, 15% rutile) to those produced by commercial flame hydrolysis processes, we assumed that LFFSP Al_2O_3 would also be similar to Al_2O_3 produced by gas-phase techniques, e.g., γ-Al_2O_3.[16,17] Furthermore, we assumed that because of the high flame temperatures, the precursor type would have very little effect on the phase of Al_2O_3 nanopowder formed.

We have now determined that precursor type has a strong effect on the quality (surface area, particle size, and phase composition, etc.) of Al_2O_3 nanopowders produced. Furthermore the nano-Al_2O_3 produced consists of a mixture of the δ^*, δ, θ, and γ phases, rather than the expected γ phase. The δ^*-Al_2O_3 lattice permits doping with unusal amounts of rare earths providing materials that exhibit incoherent lasing, "stationary light", a direct result of the powders being nanosize.[18,19] We discuss here the effects of chemical precursor on the properties of LFFSP-derived nanosized alumina powders.

Experimental Section

Four different precursors were studied: (1) alumatrane, $N(CH_2CH_2O)_3Al$[5] derived from aluminum tris-(*sec*-butoxide), $Al(OsBu)_3$, 97% (Chattem Chem.) and triethanolamine $N(CH_2CH_2OH)_3$ 98% (Aldrich); (2) aluminum acetylacetonate, $Al(Acac)_3$, 99% (Aldrich); (3) $Al(NO_3)_3 \cdot 9H_2O$, 98$^+$% (Aldrich); and (4) anhydrous $AlCl_3$ 99.99% (Aldrich). All chemicals were used as received.

Alumatrane Preparation. Alumatrane was prepared using procedures described elsewhere.[5] The product alumatrane in ethanol was analyzed by TGA for ceramic content and then diluted with a 50:50 THF/EtOH mixture to 2.5 ceramic wt %.

Solubilities. Alumatrane, aluminum nitrate, and aluminum chloride are quite soluble in 50:50 THF/EtOH mixtures, beyond the 2.5 wt % ceramic used in this study. However, $Al(Acac)_3$ exhibited poor solubility and was best dissolved in 50:50 THF/EtOH by heating to 50 °C for 1 h with stirring. On cooling, the $Al(Acac)_3$ precipitates on standing overnight. Consequently, LFFSP solutions were kept at ≈50 °C during powder production.

LFFSP Processing. The LFFSP apparatus has been described previously.[10] Typically a 2.5 wt % ceramic yield solution of precursor in a 50:50 THF/EtOH mixture is atomized at ≈50 mL/min in an ultrasonic oxygen atomizer to generate an oxygen-rich aerosol that is ignited via methane/oxygen pilot torches.[10] Combustion occurs at temperatures >1500 °C[10] followed by quenching at rates >500 °C/sec, between the combustion chamber and the 300 °C collection point (≈1.5 m). The powders are collected downstream in wire (alumel)-in-tube (Al) electrostatic precipitators (ESP), removed, and stored in plastic bags. No further effort was made to protect the powders from the atmosphere.

Heat Treatment. Selected powders were annealed using a Thermolyne Type 6000 furnace, equipped with a Eurotherm programmable temperature controller (model 818P; Northing, England).

Simultaneous Thermogravimetric and Differential Thermal Analysis. Studies were performed using a 2960 simultaneous thermogravimetric and differential thermal analyzer (SDT) (TA Instruments, Inc., New Castle, DE). Samples (≈100 mg), hand-pressed in a 3-mm dual action die, were placed in Pt sample cups and heated at rates of 2−50 °C/min to 1400 °C. The reference was a 100−mg α-alumina pellet. Synthetic air (50 mL/min) was used for all SDT experiments.

XRD Studies. As-prepared and calcined samples were characterized using: (1) a Rigaku rotating anode goniometer, (2) a Philips PW 1830 diffractometer, or a Philips X'Pert Pro diffractometer. Powder samples for the Rigaku and PW 1830 diffractometers were prepared by placing ≈100 mg in XRD sample holders (amorphous silica slides) for data collection. Cu Kα ($\lambda = 1.54$ Å) radiation with a Ni filter was used with a working voltage of 40 kV and current of 100 mA. Scans were continuous from 10 to 80° 2θ with a step scan of 2° 2θ/min and increments of 0.05° 2θ.

XRD patterns taken on the Philips PW 1830 diffractometer used sample powders packed in a glass holder. As above, filtered Cu Kα radiation was used with a working voltage of 40 kV and current of 30 mA. Scans were acquired from 10° (sometimes 5°) to 70° 2θ in increments of 0.05° 2θ with acquisition times of 2 s (1.5° 2θ/min). Peak positions and relative intensities were characterized by comparison with ICDD files for δ, δ^*, θ, and α-alumina (16−394), (23−1009), (46−1215), and (10−173), respectively.

XRD patterns taken on the Philips X'Pert Pro[20] diffractometer used the following procedure. Powders were packed in a 32-mm silicon metal low background holder.[21] These holders were used as a specimen to measure all background profiles. The diffractometer was equipped with a long fine focus copper X-ray source powered of 40 kV and 40 mA; X'Celerator detector and beam tunnel; 0.04 rad Source and receiving Soller collimators; 20-mm source mask; Degree primary slit; and Degree Anti-Scatter Slit. Scans were acquired from 4 to 145° 2θ with an increment of 0.05° 2θ and total acquisition time of 20 min [7.25° 2θ/min]. Diffraction patterns were acquired using Philips Electronics Inc. Data Collector[20] software and processed using Material Data, Inc.[22] Jade version 6.1 and Riqas version 4.0.0.8 software packages. Peak positions and relative intensities were characterized by comparison with ICDD files as above. A phase filter was prepared by including α-alumina,

(14) a. Pflanz, K. B.; Riedel, R. F.; Chmiel, H. *Adv. Mater.* **1992**, *4*, 662. b. Zhang, J.; Stauf, T. G.; Gardiner, R.; Van Buskirk, P.; Steinbeck, J. *J. Mater. Res.* **1993**, *9*, 13333. c. Mathur, S.; Veith, M.; Shen, H.; Hufner, S.; Jilavi, M. H. *Chem. Mater.* **2002**, *14*, 568. d. Veith, M.; Mathur, S.; Kareiva, A.; Jilavi, M.; Zimmer, M.; Huch, V. *J. Mater. Chem.* **1999**, *9*, 3069−3079.

(15) a. Limaye, A. U.; Helble, J. J. *J. Am. Ceram. Soc.* **2002**, *85*, 1127. b. Limaye, A. U.; Helble, J. J. *J. Am. Ceram. Soc.* **2002**, *86*, 273. c. Skandan, G.; Chen, Y−J.; Glumac, N.; Kear, B. H. *Nanostructured Mater.* **1999**, *11*, 149. d. Briesen, H.; Fuhrmann, A.; Pratsinis, S. E. *Chem. Eng. Sci.* **1998**, *53*, 4105.

(16) McHale, J. M.; Navrotsky, A.; Perrotta, A. J. *J. Phys. Chem. B* **1997**, *101*, 603.

(17) a. Glumac, N. G.; Chen, Y.-J.; Skandan, G.; Kear, B. *Mater. Lett.* **1998**, *34*, 148. b. Tani, T.; Takatori, K.; Watanabe, N.; Kamiya, N. *J. Mater. Res.* **1998**, *13*, 1099.

(18) Williams, G.; Rand, S. C.; Hinklin, T.; Laine, R. M. *Phys. Rev. A.* **2002**, *65*, 013807.

(19) Li, B.; Williams, G.; Rand, S. C.; Hinklin, T.; Laine, R. M. *Optics Lett.* **2002**, *27*, 394.

(20) Philips Analytical, P.O. Box 13, 7600 AA, Almelo, The Netherlands.

(21) The Gem Dugout, 1652 Princeton Drive, State College, PA 16803.

(22) Materials Data, Inc., 1224 Concannon Blvd., Livermore, CA 94550.

Table 1. Rietveld Modeling Parameters Used in the Phase Filter[a]

modeling parameter	α-alumina 10-173	θ-alumina 23-1009	δ-alumina 47-1292	δ-alumina 46-1131	δ*-alumina 46-1215	γ-alumina 50-0741
system	trigonal	monoclinic	cubic	tetragonal	orthorhom.	cubic
space group	$R\bar{3}c$ (167)	$C2/m$ (12)	$Fd3m$ (227)	$P\bar{4}m2$ (115)	$P222$ (16)	$Fd\bar{3}m$ #o2 (227)
a, Å	4.757	11.901	7.989	5.599	7.926	7.923
b, Å	4.757	2.899	7.989	5.599	7.961	7.923
c, Å	12.987	5.614	7.989	23.657	11.706	7.923
α, °	90	90	90	90	90	90
β, °	90	103.893	90	90	90	90
γ, °	120	90	90	90	90	90
profile shape	Pearson VII	Pearson VII	Pearson VII	Pearson VII	Pearson VII	Pearson VII
U	0.0066	0.0066	0.0066	0.0066	0.0066	0.0066
V	−0.0115	−0.0115	−0.0115	−0.0115	−0.0115	−0.0115
W	0.0135	0.0135	0.0135	0.0135	0.0135	0.0135
m_0	1.3416	1.3416	1.3416	1.3416	1.3416	1.3416
iso. temp.	0	0	0	0	0	0.4127

[a] ICDD files listed below phase.

θ-alumina, δ-alumina, δ*-alumina, and γ-alumina into a crystallographic library for Rietveld modeling.[23] The starting conditions for the major five phases are listed in Table 1.

Solid State ^{27}Al MAS NMR. These spectra were recorded at 78.2 MHz on a Bruker MSL300 spectrometer equipped with a 4-mm CP-MAS probe (spinning rate 12 kHz) and on an AVANCE 600 Bruker spectrometer equipped with a 2.5-mm CP-MAS probe (spinning rate 12−32 kHz). To ensure minimum error in the quantitation of the observed NMR peak intensities, short excitation pulses (7.5°) were used. The signal was acquired under high power proton decoupling, and recycle delays of 500 ms were used. For the cross polarization experiments, the Hartman−Hahn condition was adjusted to bohemite [AlO(OH)] with a radio frequency field of 38 kHz. Chemical shifts are externally referenced to 1 M $Al(NO_3)_3$ in aqueous solution.

The ^{27}Al NMR parameters (isotropic chemical shift value, δ_{iso}, quadrupolar coupling constant, C_Q, and asymmetry parameter, η) were calculated at the IDRIS supercomputer center of CNRS. The code PARATEC[37] was used within periodic boundary conditions and the pseudopotential approximation.[38] The all-electron electric field gradient was calculated[39] to compute the corresponding quadrupolar parameters. The quadrupolar coupling constant C_Q was extracted using an experimental value of 14×10^{-30} m^2 for the constant Q.[40] These calculations give the absolute shielding tensors and the ^{27}Al isotropic chemical shift scale was established by comparison between experimental and calculated values for α-Al_2O_3, berlinite $AlPO_4$, and 3 $SiAl_2O_5$ polymorphs.[41]

FTIR Spectra. Transmission and diffuse reflectance Fourier transform (DRIFT) spectra were recorded on a Mattson Galaxy Series FTIR 3000 spectrometer (Mattson Instruments, Inc., Madison, WI). Optical grade, random cuttings of KBr (International Crystal Laboratories, Garfield, NJ) were ground with 1.0 wt % of the sample to be analyzed. For DRIFT analysis, samples were packed firmly and leveled off at the upper edge to provide a smooth surface. For transmission IR, 100 mg of each sample prepared for DRIFT analysis was pressed in a stainless steel double action die (12.75-mm diameter) at 100 MPa for 1 min in a Carver Laboratory Press (model 3912). The FTIR sample chamber was flushed continuously with N_2 prior to data acquisition in the range 4000−400 cm^{-1}.

Specific Surface Area (SSA) Analyses. SSA data were obtained using a Micromeritics ASAP 2010 sorption analyzer. Samples (200 mg) were degassed at 400 °C/2 h. Analysis was run at −196 °C (77 K) with nitrogen gas. The SSAs were determined by the BET multipoint method using at least five data points with relative pressures of 0.001−0.20.

Scanning Electron Microscopy (SEM). SEM was done on a Philips model XL-30. Samples were dispersed in distilled water and a drop of the suspension was placed on a polished Al stub and allowed to dry. Colloidal silver was applied to improve conductivity. Powders were spark coated with carbon or sputter coated with 10−40 nm of Au−Pd to reduce charging effects. An operating voltage of 5−30.0 kV was used.

Transmission Electron Microscopy (TEM). TEM was run on a JEOL model 2010F (TEM). Samples were prepared by dipping a holey carbon grid in a vial of the as prepared powder. The specimen was held in a Gatan double tilt goniometer. An operating voltage of 200 kV was used.

Results and Discussion

Details of the LFFSP process have been published.[10] In this study, the effects of four different precursors on the formation of Al_2O_3 nanopowders were investigated. It was initially assumed that LFFSP-derived powders would have properties relatively independent of precursor source, since combustion temperatures >1500 °C[10] might be expected to generate the same gas phase species. However, after attempts to use low-cost, metal nitrate precursors unexpectedly gave highly undesir-

(23) *The Rietveld Method*; Young, R. A., Ed.; Oxford University Press: New York, 1997.
(24) Wagner, G. W.; Procell, L. R.; O'Connor, R. J.; Munavalli, S.; Carnes, C. L.; Kapoor, P. N.; Klabunde, K. J. *J. Am. Chem. Soc.* **2001**, *123*, 1636.
(25) Pell, A. S.; Pilcher, G. *Trans. Faraday Soc.* **1965**, *61*, 71.
(26) Rossini, F. D. *J. Res. NBS* **1932**, *8*, 119.
(27) Bell, N.; Rodriguez, M. *J. Nanosci. Nanotech*. Special issue on Nanomaterials and Nanoparticles, in press.
(28) Levin I.; Brandon, D. *J. Am. Ceram. Soc*. **1995**, *81*, 1995.
(29) Jayaram, V.; Levi, C. G. *Acta Metall.* **1989**, *37*, 569.
(30) Fargeot, D.; Mercurio, D.; Dauger, A. *Mater. Chem. Phys.* **1990**, *24*, 299.
(31) Oljaca, M.; Luten, H. A.; Tomov, T.; Sundell, T.; Hunt, A. *Surf. Eng*. **2003**, *19*, 457.
(32) a. Mahadevan, R.; Lee, D.; Sakurai, H.; Zachariah, M. R. *J. Phys. Chem. A* **2002**, *106*, 11083. Madler, B. L.; Pratsinis, S. E. *J. Am. Ceram. Soc.* **2002**, *85*, 1713−1718.
(33) a. Lee, D. H.; Condrate, R. A. *Mater. Lett.* **1995**, *23*, 241. b. Saniger, J. M. *Mater. Lett.* **1995**, *22*, 109. c. Tarte, P. *Spectrochim. Acta* **1967**, *23A*, 2127.
(34) Slade, R. C. T.; Southern, J. C.; Thompson, I. M. *J. Mater. Chem*. **1991**, *1*, 563.
(35) a. Fitzgerald J. J.; Piedra, G.; Dec, S. F.; Seger, M.; Maciel, G. E. *J. Am. Chem. Soc.* **1997**, *119*, 7832. b. Fitzgerald, J. J.; Piedra, G.; Dec, S. F.; Seger, M.; Maciel, G. E. *J. Am. Chem. Soc.* **1997**, *119*, 7832.
(36) Yamaguchi, G.; Yasui, I.; Chiu, W.-C. *Bull. Chem. Soc. Jpn.* **1970**, *43*, 2487.
(37) Lippens, B. C.; De Boer, J. H. *Acta Crystallogr*. **1964**, *17*, 1312.
(38) PARATEC (PARAllel Total Energy Code). Pfrommer, B.; Raczkowski, D.; Canning, A.; Louie, S. G. (with contributions from Mauri, F.; Cote, M. Yoon, Y.; Pickard, C.; Heynes, P.) Lawrence Berkeley National Laboratory: Berkeley, CA.
(39) Pickard, C. J.; Mauri, F. *Phys. Rev. B* **2001**, *63*, 245101.
(40) Profeta, M.; Mauri, F.; Pickard, C. J. *J. Am. Chem. Soc.* Submitted for publication.
(41) Pyykkö, P. *Mol. Phys.* **2001**, *99*, 1617.

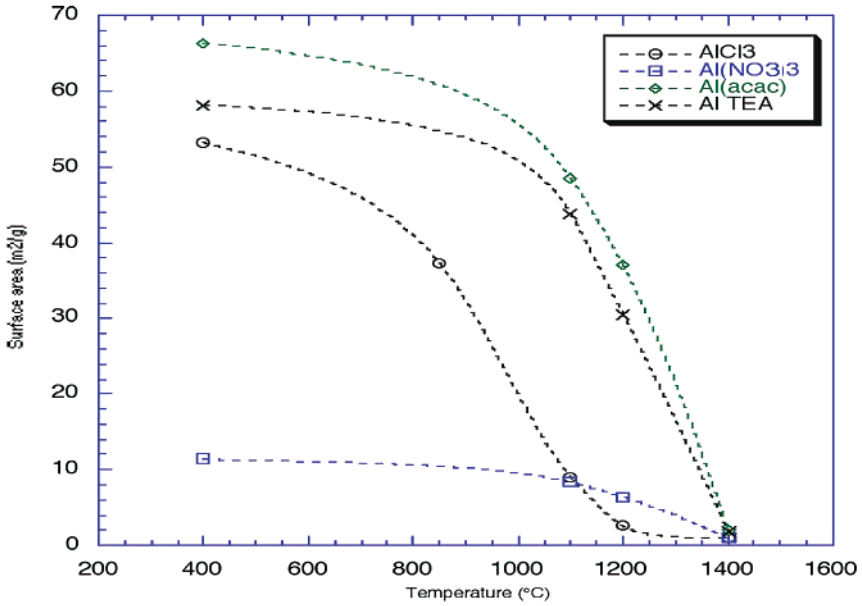

Figure 1. Surface areas of as-prepared powders and on heating to selected temperatures (10 °C/min/air/2-h hold at temperature).

able powders, we decided to investigate the roles of precursor ligands in powder formation. Furthermore, given the potential that these novel phase powders may offer as high-surface-area catalyst supports, as sorbents for chemical warfare agents,[24] and in general for numerous ceramic powder applications, we have also briefly compared selected properties of the as-produced and partially heat-treated powders.

Precursors were chosen to explore variations in ligand bonding types on powder properties. These include: alumatrane, $[N(CH_2CH_2O)_3Al]$; aluminum acetylacetonate, $Al(Acac)_3$; $Al(NO_3)_3{\cdot}9H_2O$; and anhydrous $AlCl_3$. The first two contain tri- and bidentate organic ligands, bound to Al via covalent C−O−Al links, which are expected to participate in the combustion process. In contrast, the nitrates are ionically bound to the Al. Nitrate-hydrates are known to melt easily and decompose thermally to produce NO_x species without combusting. $AlCl_3$, with more covalent than ionic Al−Cl links, was expected to hydrolyze during LFFSP. Given that the physical properties of the powders resulting from LFFSP of these four precursors are quite different, it appears that the ligand properties greatly affect particle morphology, size distribution, and surface chemistry.

Below, we first discuss particle morphology in terms of surface areas, crystallinity, and particle sizes and use these data to briefly discuss possible particle formation mechanisms. Thereafter, we characterize each powder with respect to thermal properties, surface and bulk chemistries, and lattice structure at the atomic level.

LFFSP Powder Production and Particle Morphologies. All four precursors; alumatrane, $Al(Acac)_3$, $Al(NO_3)_3$, and $AlCl_3$, are sufficiently soluble in 50:50 THF/EtOH to give a standard 2.5 wt % ceramic loading in solution. Previous LFFSP studies used only EtOH.[7−11] THF was added to ensure a fuel that dissolves all the precursors equally. The use of THF has three primary effects on LFFSP: (1) it lowers the solution viscosity providing more efficient atomization; (2) the heat of combustion or fuel value for THF, 2533 kJ/mol,[25] is higher than that of ethanol at 1366 kJ/mol;[26] and (3) THF, a less polar solvent, dissolves precursors with lower dipole moments, yet still burns with low soot production.

LFFSP precursor aerosolization and combustion are generally straightforward, except for $Al(Acac)_3$ solutions. The poorly soluble $Al(Acac)_3$ frequently precipitates in the atomization nozzle causing nozzle pressures to vary ±25%, as measured by a pressure gauge between the pump and nozzle, especially if the nozzle is cold. LFFSP of $AlCl_3$ solutions corroded all metal components; thus, only partial results are presented.

Below, the results are presented according to the techniques used (BET, SEM, and XRD, respectively) to analyze the powders. Some data are given in the Supporting Information.

Specific Surface Area (SSA) Analysis. Figure 1 plots SSA changes for as-produced powders annealed to selected temperatures between 400 and 1400 °C. SSAs of the as-produced Al_2O_3 are 66, 58, 53, and 12 m^2/g for $Al(Acac)_3$, alumatrane, $AlCl_3$, and $Al(NO_3)_3$, respectively. The 53 m^2/g found for the $AlCl_3$ sample does not correspond to the particle sizes observed by SEM and falls off rapidly above 850 °C. Significant unreacted $AlCl_3$ remains in the particles, which sublimes during the BET measurement process, as suggested by the TGA studies below.

Heat treatments to 1200 °C (10 °C/min/air/2 h hold) convert all of the powders to α-alumina. The $Al(Acac)_3$ and alumatrane powders retain SSAs of 37 and 31 m^2/g, respectively. These results suggest potential utility as catalyst supports, especially because of the absence of microporosity. In contrast, the $AlCl_3$ and $Al(NO_3)_3$ derived powders have SSAs < 5 m^2/g.

Scanning Electron Microscopy (SEM). SEM micrographs of as-prepared powders are shown in Figure 2. The morphologies of the $AlCl_3$ and $Al(NO_3)_3$ powders (Figure 2a and b) are similar, with a majority of the particles in the 1-μm diameter range, with a small population of particles of <100 nm. The $Al(NO_3)_3$–derived powders also appear to contain a significant number of hollow particles, as evidenced by their dark interiors.

In contrast, the alumatrane- and $Al(Acac)_3$-derived powders, Figure 2c and d, have very similar average

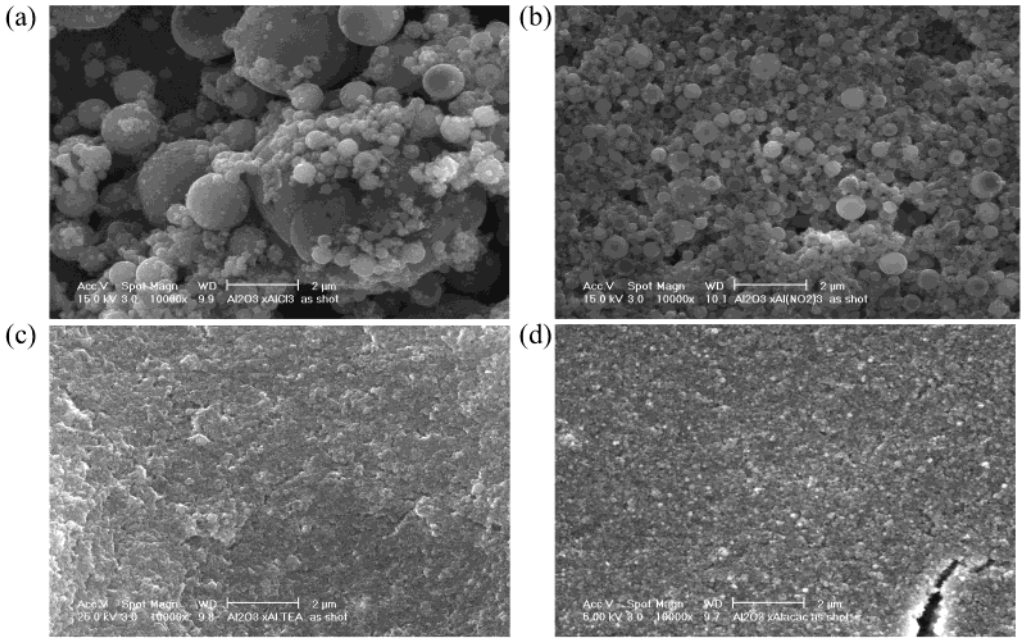

Figure 2. SEM pictures of Al_2O_3 particles derived from (a) $AlCl_3$; (b) $Al(NO_3)_3$; (c) alumatrane; and (d) $Al(Acac)_3$ (scale bar 2 μm).

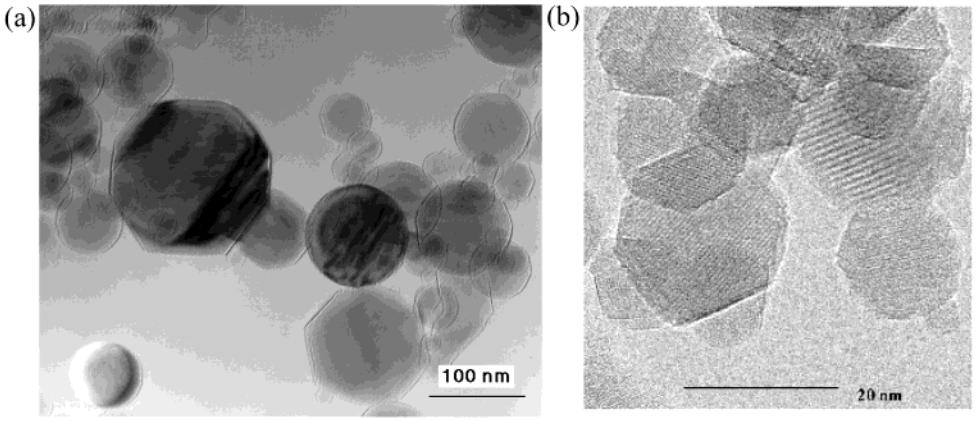

Figure 3. TEM images of alumatrane-derived nanopowders at 5 wt. % (a) and 1 wt % (b) in EtOH. In the latter image, the particles are also doped with 3000 ppm Ce^{3+}.[18,19]

particle sizes (APSs) and morphologies, which remain unchanged on heating below the α-alumina conversion temperature. However, above 1200 °C, both powders coarsen with APSs of 300 nm and form hard agglomerates (images not shown).

Transmission Electron Microscopy (TEM). TEM images of facetted particles produced from 5 and 1 wt % ceramic yield alumatrane in EtOH, respectively, are presented in Figure 3. Facetting is indicative of crystallinity as borne out by XRD studies below. The dark lines seen on the larger particles in Figure 3a may result from stacking faults or step growth planes. The relatively spherical particle shapes may indicate formation of molten droplets during LFFSP. During revision of this paper, Nelson and Rodriguez found that as-prepared LFFSP alumina (alumatrane) disperses easily in water with no evidence for necking or agglomerate formation.[27] One might argue that the absence of necking or agglomerates, as found for LFFSP-produced mullite composition particles,[8] implies that molten droplets do not form. This is discussed in detail below.

X-ray Powder Diffraction Patterns (XRDs). XRDs of the as-prepared materials are all very similar. Analysis of the patterns in the 0 to 30° 2θ region indicates the presence of three possible crystalline forms: δ (tetragonal), θ, and δ*-Al_2O_3. However, delineation between these phases using only the long-range order information from the 0 to 30° 2θ range is extremely challenging.

The two phases present quite analogous diffraction patterns, except in the 20−30° range, where no diffraction peak due to θ−Al_2O_3 is present.

This is illustrated in Figure 4, which suggests that the nitrate-derived powders are primarily δ-Al_2O_3. However, the alumatrane-derived powders appear to be mixtures of both δ and θ-Al_2O_3. The $Al(Acac)_3$-derived powders are similar and thus not shown.

The difficulty in analysis is also partly attributable to the very fine crystallite sizes, which broaden the XRD considerably. Consequently, we resorted to Rietveld refinement to better characterize the phase composition. Figure 5 shows data for the alumatrane-derived powders. Rietveld refinement[23] involves the use of crystal structure data to calculate a theoretical XRD pattern so that the difference between the theoretical and measured patterns can be used to better understand the

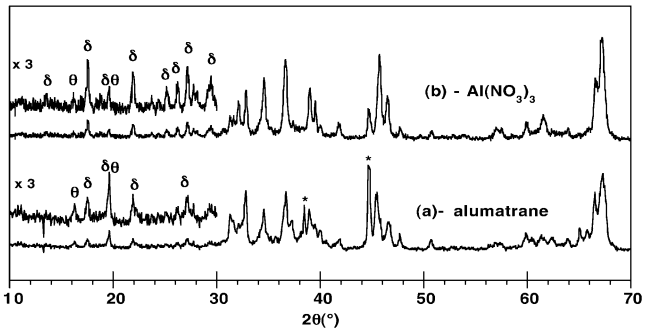

Figure 4. XRD patterns of as-prepared powders derived from (a) alumatrane and (b) aluminum nitrate. (*Al sample holder).

physical and chemical makeup of the sample. Rietveld phase filtering allows a broad range of possible crystal structures to be evaluated as potential constituents of a sample. Because aluminas can be complex mixtures of phases with various degrees of crystallinity, a phase filter was assembled that included tetragonal δ, cubic δ, δ*, θ, γ, and α-Al_2O_3 as potential components of the measured diffraction pattern per Table 1.

The alumatrane phase filter analysis shown in Figure 5 indicates that cubic δ, θ, γ, and δ*-Al_2O_3 are all present. It is important to note, and not readily apparent, using the 0 to 30° 2θ diffraction information, that δ*-alumina is the primary crystalline constituent. The advantage of phase assignment using Rietveld refinement with phase filtering is that the entire diffraction pattern is used to assess the validity of a phase assignment. Therefore, ambiguity in the long-range order dominated by the low-angle region of the diffraction pattern can be overcome using short-range order information present in the 70−140° 2θ region. The use of 70−140° 2θ information has typically been limited by the availability of high-resolution, high-speed diffractometers.

Note that the phases show different peak widths associated with a range of crystallite sizes for each component. The corresponding phase composition and crystallite domain size indicates the complex nature of the sample and is a good example of the difficulty in obtaining pure-phase aluminas with a single morphology. In essence, at the current state of interpretation, these four phases with their respective weight fractions and crystallite domain sizes best describe the XRD pattern. The residual plot just below the diffraction pattern in Figure 5 demonstrates the importance of Rietveld modeling with phase filters. The residuals in this trace indicate that there is potentially more information to learn about the alumatrane material.

Metastable Al_2O_3 structures can be divided in two broad categories: a face-centered cubic (fcc) or a hexagonal close-packed (hcp) arrangement of oxygen anions.[28] The structures based on fcc packing of oxygen include γ, η (cubic), θ (monoclinic), and δ (cubic or tetragonal). Among them, γ-alumina appears to be the most thermodynamically stable phase for Al_2O_3 nanopowders.[16] The fact that we produced nanopowders that are δ*-alumina with cubic δ, γ, and θ-alumina is likely because our process is driven by kinetics rather than thermodynamics. The formation of a δ*-alumina phase is not unprecedented in high-temperature gas-phase processes. The reference material given in ICDD file 46-1215 was produced via a plasma process. The different product morphologies and phases likely arise as a combination of precursor behavior on initial heatup, combustion, highest flame temperature, and quench rate, as discussed in the next section. Note that formation of δ*-alumina seems to be favored by LFFSP and plasma processes that experience rapid quenching and where considerable water is involved.[29,30]

To understand the thermal behavior of the as-prepared powders, XRD analyses of alumatrane-derived powder heated to selected temperatures were conducted to follow phase evolution, per Figure 6. Powders heated to 750 °C retain the original phase structure, but at 1000 °C the peaks sharpen and θ-Al_2O_3 becomes the

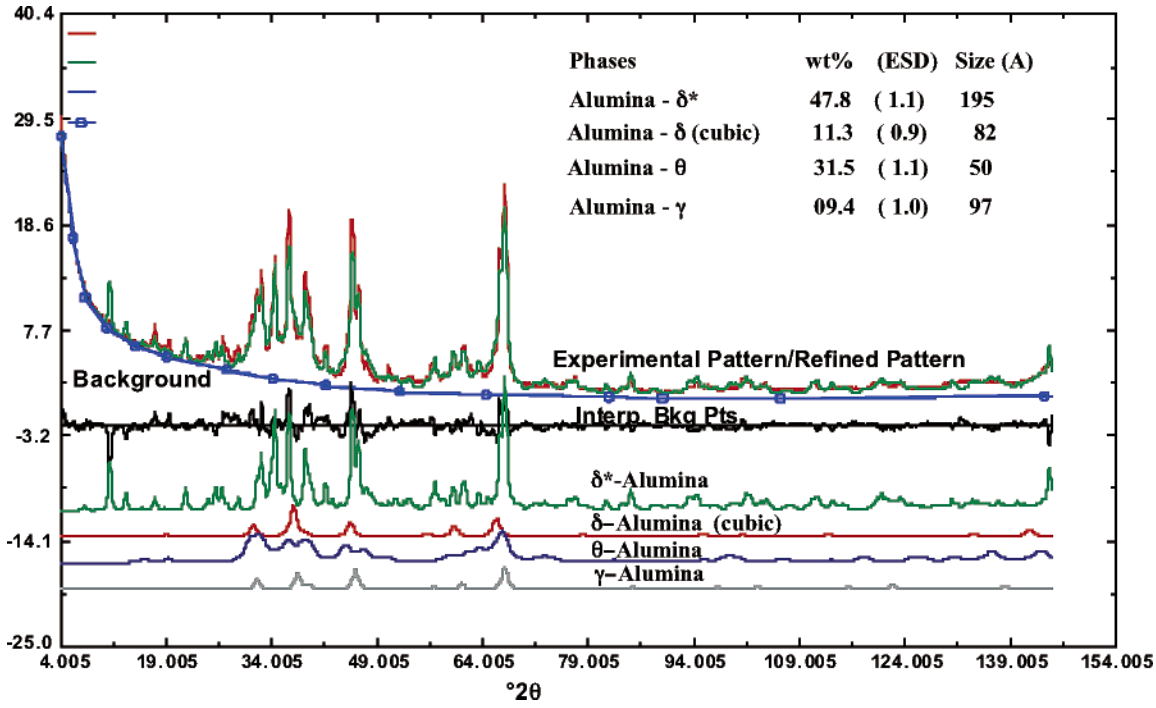

Figure 5. Rietveld refinement of alumatrane-derived powders.

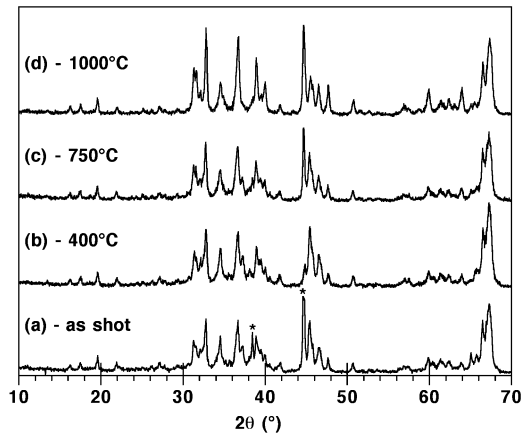

Figure 6. XRD patterns of as-prepared (shot) alumatrane-derived alumina heated to selected temperatures (10 °C/min/air/2-h hold).

Table 2. APSs for Precursor-Derived Nanoaluminas (nm ± 3 nm)

precursor	$Al(NO_3)_3$	alumatrane	$Al(Acac)_3$	$AlCl_3$
BET[a]	70	14	13	16
XRD[b]		<20		

[a] From SSAs. $AlCl_3$ data obtained following sublimation of excess $AlCl_3$. [b] From Figure 5 Rietveld analysis.

dominant phase. Weak peaks between 20 and 30° suggest that some δ- or δ*-Al_2O_3 remains. At 1200 °C, conversion to α- Al_2O_3 is complete.

The δ to θ to α transformations are often observed for fcc Al_2O_3 polymorphs.[28] The δ*-Al_2O_3 phase was originally described as a transitory phase produced in the synthesis of δ-Al_2O_3. Therefore, it is logical to believe that δ*-Al_2O_3 would produce θ-Al_2O_3 along the pathway to α-Al_2O_3. θ-Al_2O_3 is also a significant weight fraction of the as-prepared sample per Rietveld refinement. Combining the Rietveld analyses and the BET derived SSAs, Table 2 lists the calculated particle sizes for the various samples.

Particle Formation Processes. On aerosolization, the precursor solution droplet sizes are typically 1−20 μm.[10] The combustion process is assumed to be similar to combustion of oil droplets. Thus, as the resulting droplets heat in the flame, solvent evaporation begins and vapor near the surface starts to combust. As the local temperature exceeds the solvent boiling point, the original droplets will fragment. Particle formation likely involves combustion of these fragments. The various processes, including droplet evaporation, burning, and fragmentation, resulting in hollow spheres, dense particles, and particle fragments have been discussed by us previously,[8,10] and also by Helble,[15a,b] Oljaca et al.,[31] and Zachariah et al.[32]

If organic ligands are present, they should combust coincidentally resulting in atoms, ions, hydroxyl, and oxide ions of Al. Oljaca et al. observe similar species for Ba-, Sr-, and Ti-containing flames produced via LFFSP.[31] Shortly thereafter, only oxo and hydroxyl species will remain in the oxygen-rich flame, which can then form clusters, nuclei, and finally particles. The thermal decomposition pattern (TGA/air) of the alumatrane has been described already, it oxidizes completely to Al_2O_3 at ≈400 °C.[5] Unfortunately, the $Al(Acac)_3$ material sublimes (TGA/air) before it fully decomposes and therefore its thermal decomposition behavior cannot be determined with any confidence.

LFFSP flame temperatures have been determined from calculations of feed-gas flow rate, and chemical makeup (fuel values[25,26]).[10,15,31] In addition, they have been estimated using thermocouples directly downstream of the combustion chamber, as described in detail previously.[10]

The thermodynamics and kinetics that control particle growth processes are beyond the scope of the work discussed here. However, some comments can be made about particle formation on the basis of our observations and what is known in the literature.

As noted above, Bell and Rodriquez saw no evidence of agglomerate formation.[27] In addition to the above TEMs, those in the Bell paper show no evidence of necking. For necking or agglomeration to occur, as-formed particles must coalesce to some extent following one or just a few collisions. Because no necks or agglomerates appear, two particle formation scenarios are likely.

If the flames are quenched at high rates, then the number of collisions at temperatures sufficient for necking or agglomeration will be minimal and the products observed are purely a result of gas-phase particle growth. This would explain why the composition of the precursor solution is preserved in mixed-metal oxide nanopowders.[8−13] Alternately, the particles could coalesce so fast that no necking or hard agglomerates form before temperatures are too cool for even adhesion to occur. This would lead to more spherical particles. We cannot distinguish between these possibilities at present.

The nitrate and chloride systems have completely different chemistries and therefore different kinetics and thermodynamics. Nitrates decompose relatively rapidly but also melt before they decompose.[32] In contrast, chlorides must hydrolyze before particles form.[1−3] From Figure 2b, and studies by Zachariah et al. and Madler et al. on nitrate behavior under spray pyrolysis conditions, it appears that at least partial nitrate melting occurs during the LFFSP heat-up process, before decomposition.[32] Partial melting leads to coalescence to bigger particles. Hollow particles (see Figure 3 in Supporting Information), as seen for the nitrates, are commonly observed in spray pyrolysis.[1−3,32]

One final issue relates to the alumina phases observed. The high-temperature alumina phase, hexagonal α-alumina (3.99 g/cm^3), should form at LFFSP temperatures. However, we see only δ*-alumina (3.8 g/cm^3), cubic δ (3.5 g/cm^3), and θ-alumina (3.2 g/cm^3). It can be argued that the formation of δ/δ*/θ-mixtures might be favored simply on the grounds that lower densities reduce the unit surface area free energies of these small, highly curved particles thereby stabilizing them. A direct consequence of the larger unit cell parameters (Table 2) is that these powders are better able to accommodate rare earths ions in the lattice, providing novel photonic materials.[18,19]

Water may also play a role in stabilizing the δ-phase. However, McHale et al. reported that water stabilizes nanostructured θ- and α-Al_2O_3 almost equally, suggesting it actually plays little role in phase stability.[16]

Thermal Properties, Surface and Bulk Chemistries, and Lattice Structure. Thermal analysis studies of as-produced powders should provide an indication

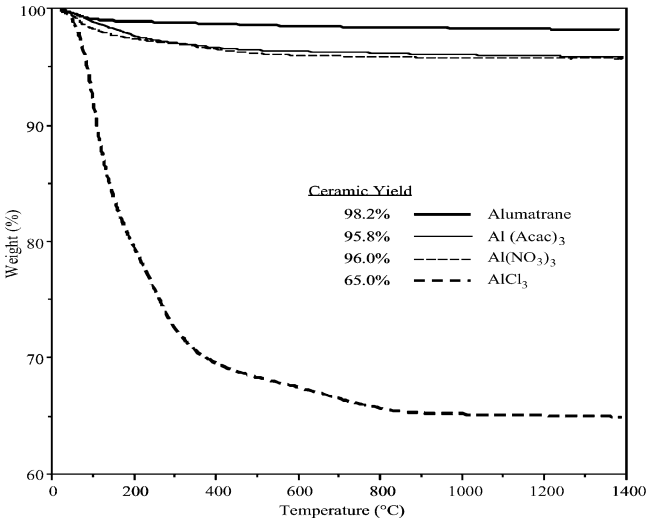

Figure 7. TGAs of as-prepared powders from four different precursors, 10 °C/min/air.

of their potential utility for catalyst support applications. Coincidentally, the surface chemistry of the as-prepared powders is best characterized by combining thermal analysis with diffuse reflectance FTIR. Bulk atomic interactions are best characterized using transmission IR coupled to solid-state NMR. Solid-state NMR can also provide some information about surface chemistry through proton coupling studies.

Thermal Gravimetric Analyses. Results of TGA of the four as-prepared powers are shown in Figure 7.

Powders derived from alumatrane, $Al(Acac)_3$, and $Al(NO_3)_3$ exhibit typical 1−3 wt % mass-loss behavior over the 1000 °C ramp range. These values correspond to a few monolayers of surface species including physi- and chemisorbed water and some carbonate species (see FTIR studies in the Supporting Information).[16] The alumatrane-derived powders, with an SSA of 58 m^2/g have a mass loss of 1.8 wt. %. This amount of water appears to be much less than that found by McHale et al. in studies on the hydration of nanosized γ- and α-alumina.[16] The differences are likely a consequence of the fact that the current materials are produced in a kinetically controlled process rather than under equilibrium conditions. Also, the current materials do not exhibit any microporosity, which could also greatly affect bulk hydration behavior.

In contrast, the $AlCl_3$ derived powders undergo a 35% mass loss on heating, most likely because $AlCl_3$ sublimes at atmospheric pressures at 178 °C (CRC Handbook).

Differential Thermal Analysis. In Figure 8, both the $Al(Acac)_3$- and $Al(NO_3)_3$-derived powders have similar α-alumina peak crystallization temperatures of 1240 °C.

Alumatrane-derived powders crystallize to α-alumina at ∼1260 °C. The crystallization exotherm for the $Al(NO_3)_3$-derived powder is broader and less intense with a 20 °C earlier onset. One likely explanation is that the finer powders are more hydrated and thus more energy is needed to drive off the final hydroxyl groups before crystallization can occur.[16] $AlCl_3$-derived powders behave quite differently because considerable unreacted $AlCl_3$ sublimes off upon heating.

FTIR. FTIR spectra of the as-prepared powders are relatively straightforward and as such discussion of the results is provided only in the Supporting Information.[33]

Solid-State ^{27}Al NMR studies. The ^{27}Al MAS NMR spectra for the as-prepared alumatrane- and nitrate-derived powders, recorded in a 7.05 T field, show both tetrahedral and octahedral Al^{3+}, as expected for transition δ- and θ-aluminas.[34,35] The $\{^1H\}$-^{27}Al CP MAS NMR spectrum recorded on the alumatrane-derived sample (Figure 9) shows only octahedrally coordinated Al^{3+}, which should be present at the surface probably as Al−OH species, while all tetrahedral Al^{3+} sites are part of the alumina lattice, far from protons.

The spectra recorded on the alumatrane-derived samples after heat-treatment (400, 750, and 1000 °C)

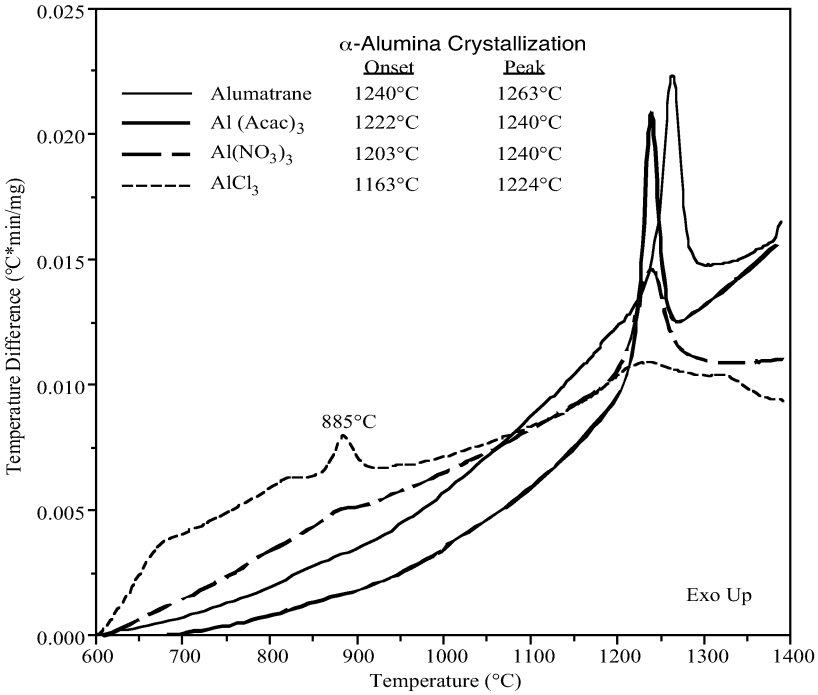

Figure 8. DTAs of as-prepared powders from four different Al_2O_3 precursors, 10 °C/min ramp.

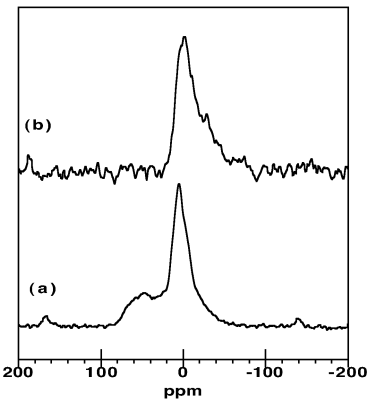

Figure 9. ^{27}Al MAS NMR spectra of as-prepared powders derived from alumatrane: (a) one pulse experiment and (b) cross polarization experiment with 500-μs contact time (magnetic field 7.05 T; MAS spinning rate 12 kHz).

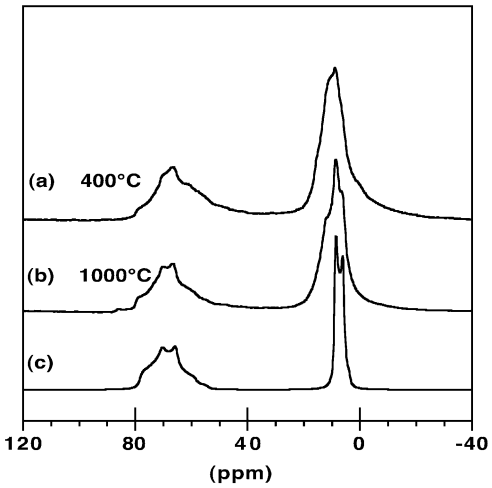

Figure 10. ^{27}Al MAS NMR spectra of alumatrane powders heated to (a) 400 °C and (b) 1000 °C (magnetic field 14.1 T; MAS spinning rate 32 kHz); (c) spectrum calculated for θ-Al_2O_3.

show few changes except for a noticeable sharpening of the peaks at 1000 °C. To gain resolution, the 400°C and 1000 °C samples were also run in a 14.1 T magnetic field (Figure 10), which confirms the presence of only tetrahedral and octahedral environments, with no evidence for five-coordinate Al^{3+}, whose signal is expected around 35 ppm.[35]

The spectrum obtained at 1000 °C shows an extremely well-defined quadrupolar shape for the signal due to tetrahedral Al sites, and distinct discontinuities for the signal due to octahedral Al sites suggesting a well-defined local order for the various Al sites. This is quite unusual for metastable alumina polymorphs, which are often characterized by distribution of Al sites due to the presence of Al vacancies in the structure. One exception is the θ-polymorph with monoclinic symmetry (space group $C2/m$)[37] which is based on two types of Al polyhedra in a 1:1 ratio: 1 tetrahedral Al(IV)/1 octahedral Al(VI). To our knowledge, the ^{27}Al NMR spectrum of this phase has not been described in the literature and provided motivation for the following efforts.

We performed ab initio calculations of the ^{27}Al NMR parameters (isotropic chemical shift value, δ_{iso}, quadrupolar coupling constant, C_Q, and asymmetry parameter, (η), of θ-alumina, based on the published crystalline structure.[35] Some details on the calculations are given in the Experimental Section. The results obtained for the two Al^{3+} sites present in θ-alumina are summarized in Table 3.

Table 3. Calculated ^{27}Al NMR Parameters Corresponding to the Two Al Sites in θ-Al_2O_3

site	δ_{iso} (ppm)	C_Q (MHz)	η
Al (VI)	9.5	3.2	0.1
Al (IV)	79.0	6.2	0.6

The corresponding spectrum is presented in Figure 10c. There is a remarkable agreement between the experimental and calculated signal due to Al(IV) sites, whereas the calculated signal due to Al(VI) corresponds only partially to the experimental signal. However, the discontinuities of the calculated quadrupolar shape coincide with the experimentally observed ones. These results show that θ-Al_2O_3 is truly the predominant phase in samples heated to 1000 °C, in agreement with the XRD data. The NMR data show also the presence of an additional phase based predominantly on octahedrally coordinated Al sites; these sites could correspond to the presence of δ-Al_2O_3. Thus, these studies corroborate the Rietveld refinement results described above.

Finally, these studies serve as a benchmark for current, ongoing efforts wherein we find that the addition of just a few percent $Ce^{3+/4+}$ cations can stablize the δ phase, such that its transformation to the α-phase can be retarded by several hundred degrees, suggesting again that these materials offer significant potential as catalyst supports.[42]

Conclusions

Aerosol combustion of metalloorganic and inorganic Al_2O_3 precursors dissolved in EtOH/THF solutions leads to quite different Al_2O_3 nanopowder combustion products. $AlCl_3$ and $Al(NO_3)_3{\cdot}9H_2O$ do not volatilize effectively under conditions where alumatrane and $Al(Acac)_3$ provide high-quality, high-surface-area Al_2O_3 powders. Apparently nitrate droplets melt during the combustion process rather than volatilize, leading to formation of large, hollow particles. In contrast, $AlCl_3$ volatilizes easily but does not hydrolyze rapidly in the flame, leading to recovered starting material. The best powders, with particle sizes <20 nm and corresponding surface areas of ≈ 60 m^2/g, are produced from alumatrane and $Al(Acac)_3$.

The LFFSP process provides Al_2O_3 nanopowders with highly hydroxylated surfaces that provide good dispersibility,[27] which offers potential for formulating catalyst supports and processing ceramic materials, as we will discuss in the future. These materials consist of a mixture of transition alumina phases that could be successfully identified and quantified only by Rietveld refinement. Solid state ^{27}Al NMR was used successfully to identify the magnetic environments of the Al atoms in these materials and the solid-state NMR of the θ phase was successfully modeled using a new modeling program.

Several issues still remain to be explored. The exact mechanism whereby the particles nucleate and grow

(42) Kim, M.; Hinklin, T.; Laine, R. M. unpublished work.

from the species generated during combustion remains unknown. Furthermore, the mechanism(s) for phase formation remain unknown, it is not clear whether a molten-phase or a gas-phase process (or both) mediates particle formation.

Acknowledgment. We thank Dr. J. Jiang and Professor X. Pan of our Department for taking the TEM images shown here. T.H. thanks NSF (IGERT grant DGE-9972776) for a fellowship and R.M.L. thanks NSF (DMR 9975542), the Army Research Office (DAAD 19-99-1-0229), and the Air Force Office of Scientific Research (F49620-03-1-0389) for partial support of this work.

Supporting Information Available: FTIR spectra of as-prepared nanoaluminas; DRIFTS spectra of heat-treated nanoalumina; SEM blow-up of hollow particles. This material is available free of charge via the Internet at http://pubs.acs.org.

CM021782T